

Effect of sintering temperature on mechanical and bioactivity properties of bioactive glass and cordierite composite

A. K. Fakhruddin¹, H. Mohamad^{1*}

¹Universiti Sains Malaysia, School of Materials and Mineral Resources Engineering, Biomaterial Research Niche Group, 14300 Nibong Tebal, Penang, Malaysia

Abstract

In this study, a composite of bioactive glass (BG) and cordierite (BG-cord) was proposed to increase the strength and bioactivity of BG. Both BG and cordierite were separately synthesized with the method of glass melting, then, they were used to fabricate BG-cord with a variation of sintering temperature (600 to 1000 °C). The highest diametral tensile strength (DTS=30.54 MPa) was shown by the BG-cord with sintering temperature at 925 °C. Bioactivity tests were conducted by soaking in Hank's balanced salt solution (HBSS) for 7, 14, and 21 days. Apatite formation was examined by using a scanning electron microscope. The results showed that the sample showed good bioactivity with regards to the formation of apatite on the samples, confirmed by the detection of carbonate (C-O) and phosphate (P-O) absorption peaks by Fourier transform infrared spectroscopy and crystalline peaks in the X-ray diffraction pattern.

Keywords: bioactive glass, cordierite, sintering temperature, bioactivity, apatite formation.

INTRODUCTION

Bioactive glass (BG) is a group of glass first invented in the late 1960s by Hench and colleagues through the introduction of 45S5 (in wt%: 45SiO₂-24.5CaO-24.5Na₂O-6P₂O₅). BG is among the preferred materials for clinical treatment applications particularly bone regeneration [1], tooth repair [2], and drug delivery [3]. BG is commonly fabricated as a powder [4], metal coating [5], or scaffolds to adapt with the damaged areas [6]. The unique properties of BG that make it outstanding among other materials are good bioactivity [7], the ability to support cell growth [8], and rapid decomposition [9]. In implant applications, BG demonstrates the capability to tightly bond an artificial material with living tissues such as bone through the formation of a biologically active crystalline apatite layer with properties similar to bone minerals, making it able to integrate with bone tissues [10]. The development of a strong bond between BG and bone results from apatite crystallization on the BG surface in reaction with body fluid [11]. The presence of silica-hydroxyl rich layer (Si-OH) on the BG surface and the dissolution of calcium and phosphate ions from BG greatly contribute to the apatite crystallization [12]. In addition, the silica-hydroxyl layer is formed with an amorphous CaO-P₂O₅ layer that crystallizes and forms an apatite layer [13]. Studies revealed that BG is more fragile and vulnerable to catastrophic failure than most previously reported materials, rendering it inconvenient for load-bearing applications [14, 15]. In addition to being fragile when fractured, BG demonstrates lower toughness and elastic modulus properties than the

human cortical bone [16]. This is evident from the failure of the BG implant taking place due to fracture at the BG-bone interface. An interesting and feasible solution to solve this issue is through the integration of cordierite into BG to form a composite with enhanced mechanical strength.

As an alternative to BG, cordierite is categorized as a crystalline ceramic material of the MgO-Al₂O₃-SiO₂ ternary system. Cordierite was chosen due to its excellent chemical resistance and mechanical properties (~243 MPa) [17]. The suitability of cordierite as a biomaterial was proven by Mengucci et al. [18], particularly in the shape of a sintered honeycomb monolith. In addition to its low production costs, cell growth can be seen as the best option to improve the mechanical and chemical resistance, insolubility, and porosity of cells. In view of this, Krajewski et al. [19] revealed that cordierite can effectively encourage cell growth. Moreover, the presence of magnesium ions (Mg²⁺) in a cordierite composition could promote cell binding through a positive response between the surface electrostatic charge and the potential cell membrane in the body [20]. Magnesium is an essential trace element that exists in the human body, thus it plays a major role particularly in bone growth and preservation, as well as providing good osteoconductivity over time [21]. The introduction of cordierite into BG is expected to enhance the properties of a ceramic composite material, hence the mechanical strength of the composite. The sintering temperature is among the significant parameters that affect the composite properties. Therefore, the purpose of this research is to determine the effect of sintering temperature on the compressive strength of bioactive glass-cordierite (BG-cord) composite. In addition, the bioactivity efficiency of the BG-cord composite was evaluated since sintering temperature also has a significant influence on bioactivity.

*hasmaliza@usm.my

 <https://orcid.org/0000-0002-7365-2267>

MATERIALS AND METHODS

Sample preparation. Synthesis of 45S5 BG and cordierite: the glass melting method was used to synthesize BG and cordierite. The 45S5 bioactive glass composition (45 wt% SiO₂, 24.5 wt% CaO, 24.5 wt% Na₂O, and 6 wt% P₂O₅) was mainly used for the synthesis. High purity silicon dioxide (SiO₂, 99.5%, Ipoh Ceramic, Malaysia), phosphorus pentoxide (P₂O₅, 99%, Fluka, Italy), calcium carbonate (CaCO₃, 99.95%, Merck, USA), as a source of CaO, and sodium carbonate (Na₂CO₃, 99.9%, Merck, USA), as a source of Na₂O, powders were mixed for 24 h in a polyethylene (PE) bottle at 25 rpm. The powder mixture was then melted in an alumina crucible at 1400 °C for a period of 1 h before the distilled water was used to quench it. Next, the glass frit obtained after quenching was dried, then the produced BG frit was milled into fine BG powder. The cordierite was synthesized using a mixture of aluminum dioxide (Al₂O₃, 99.5%, Fluka, Italy), magnesium oxide (MgO, 98%, Qrec, New Zealand), and silicon dioxide (SiO₂, 99.5%, Ipoh Ceramic, Malaysia) powders. All the raw materials were homogenously mixed together for 24 h in a PE bottle by rolling at 25 rpm. The mix of the raw materials was melted for 4 h at 1550 °C in an alumina crucible, then it was quenched in distilled water. To obtain the cordierite powder, it was dried, then ground for 15 min. After that, the powder was calcined to form crystalline cordierite at 980 °C for 2 h of soaking time. Then the cordierite was milled for another 3 h.

Fabrication of BG-cord: 70 wt% of BG and 30 wt% of cordierite from synthesized BG and cordierite powders were mixed in PE bottles for 6 h at 25 rpm. The mixture of powders was pressed to pellet shape with 13 mm diameter using a hydraulic press at 650 MPa, then, sintered at various temperatures (600 to 1000 °C). The sample notation of different sintering temperatures of BG-cord applied in this research study is tabulated in Table I.

Characterization. Particle size analysis: prior to the fabrication of the BG-cord composite, the particle size of both BG and cordierite was evaluated by analyzing the milled frit using a dry particle size analyzer (Sympatec, Helos, England). **Shrinkage:** the shrinkage of composite samples was determined by the measurement of the diameter of samples before (D_o) and after (D_s) sintering and calculated by:

$$\text{Shrinkage} = \frac{D_o - D_s}{D_o} \cdot 100 \quad (\text{A})$$

Porosity: the porosity of the composite was evaluated using a measurement method based on Archimedes' principle, where the weight of displaced fluid by a sample is equivalent to its apparent weight. In this test, the dry composite sample was weighed (M_d), then the composite sample was incubated in a desiccator for 1 h in distilled water and vacuum to ensure its pores were filled with water. The sample was then suspended in a beaker containing water (ρ=1 g/cm³) while being attached to a nylon string and the measurement taken (M_s). Subsequently, the sample was cleaned and weighed (M_w). The bulk density and porosity of the sample were determined by:

$$\text{Bulk density} = \frac{M_d}{M_w - M_s} \cdot \rho_{\text{water}} \quad (\text{B})$$

$$\text{Apparent porosity} = \frac{M_w - M_d}{M_w - M_s} \cdot 100\% \quad (\text{C})$$

Diametral tensile strength (DTS): the mechanical property of the BG-cord composite was assessed via a diametral tensile strength (DTS) test (mod. 3367, Instron, USA) using a crosshead speed of 0.5 mm/min and a load cell of 5 kN, as recommended by the ASTM-D3967; 5 samples were tested. The calculation for DTS is presented in Eq. D, where P is the applied force, D is the diameter of the sample, and T the thickness of the sample:

$$\text{DTS} = \frac{2 \cdot P}{\pi \cdot D \cdot T} \quad (\text{D})$$

Bioactivity: the biocompatibility performance of the composite was examined using *in vitro* testing by incubating BG-cord pellets in Hank's balanced salt solution (HBSS) at 37 °C for a period of 7 to 21 days in a water bath. The HBSS used in this research was supplied by Life Technologies. A cylinder containing the sample was then soaked in a 50 mL centrifuge tube. The volume of HBSS used was calculated using Eq. E, where V_s is the total volume of the HBSS required and S_a is the total surface area of the sample. At the end of the test, the BG-cord samples were carefully collected and dried at room temperature. The bioactivity performance of the samples was determined from the analyses of Fourier transform infrared spectroscopy (FTIR) and X-ray diffraction (XRD), while their surface morphology was analyzed via scanning electron microscopy (SEM).

$$V_s = 100 \cdot S_a \quad (\text{E})$$

Table I - Sample notation of BG-cord with different sintering temperatures.

Sample	BG-C600	BG-C800	BG-C850	BG-C900	BG-C925	BG-C950	BG-C1000
Sintering temperature (°C)	600	800	850	900	925	950	1000

Table II - Composition of Hank's balanced salt solution.

Reagent	NaCl	KCl	Na ₂ HPO ₄	KH ₂ PO ₄	CaCl ₂	MgSO ₄	NaHCO ₃
Content (M)	0.137	5.4m	0.25m	0.44m	1.3m	1.0m	4.2m

RESULTS AND DISCUSSION

Particle size analysis: prior to the BG-cord composite fabrication, the particle size of the BG and cordierite powders was analyzed. The particle size distribution graph is presented in Fig. 1. The largest and median particle sizes analyzed of the BG and cordierite powders after milling are tabulated in Table III. The BG powder was found to have a smaller particle size than cordierite. This was because of the composition disparity between BG and cordierite with amorphous and crystalline (orthorhombic) atomic structures, respectively [22]. A material with an amorphous structure is easier to crush than the one with a crystalline structure since the atoms in an amorphous structure are more likely to slide when a force is applied during milling than a packed and arranged atomic structure which is much harder to crush. Table III illustrates that both BG and cordierite powders' particle sizes were smaller than $38 \mu\text{m}$ at D_{100} , significant in bioactive function. Smaller particle size promotes a higher specific surface area, promoting accelerated ion diffusion due to the quick dissolution of ions such as Si^{4+} and Ca^{2+} , which impacts the bioactivity performance degree at the implant interface. Furthermore, materials with a particle size smaller than $38 \mu\text{m}$ are required for cell culture mediation as cells sizes are often in the range of $4\text{-}40 \mu\text{m}$ [4].

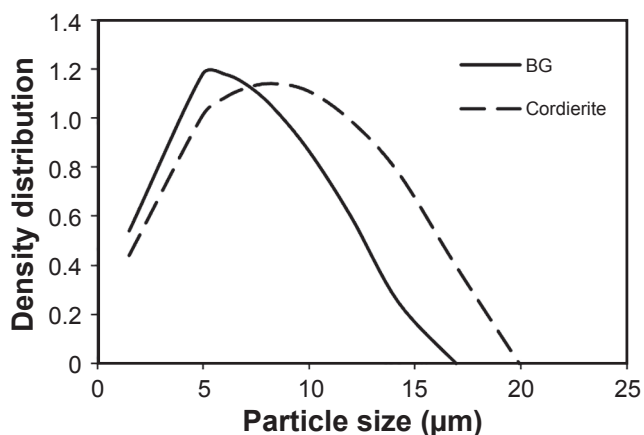


Figure 1: Particle size distribution curves of BG and cordierite powders after milling.

Table III - Largest and median particle sizes of BG and cordierite powders after milling.

Powder	Largest particle size, D_{100} (μm)	Median particle size, D_{50} (μm)
BG	16.93	4.35
Cordierite	19.94	5.45

X-ray diffraction: the phases present in the powder were analyzed using XRD analysis. Fig. 2 shows the XRD result of BG. Based on Fig. 2, an amorphous structure was observed for BG composition with a broad hump between 25° and 35° in the pattern. The temperature of 1400°C used during glass melting also was sufficient to melt the

oxide raw materials based on 45S5 BG composition. It also showed that the rapid cooling of the molten glass through quenching in distilled water was enough to prevent the crystallization process. XRD patterns for cordierite powder before and after calcining are presented in Fig. 3. An amorphous structure was observed after melting with an amorphous hump between 25° and 35° in the pattern (Fig. 3a). This showed that the raw materials of cordierite glass frit were transformed to an amorphous phase. The atoms in the glass were randomly moved during the melting process. Meanwhile, Fig. 3b shows that the major crystalline phase that occurred after calcining at 980°C was the cordierite phase (ICSD 98-001-7002).

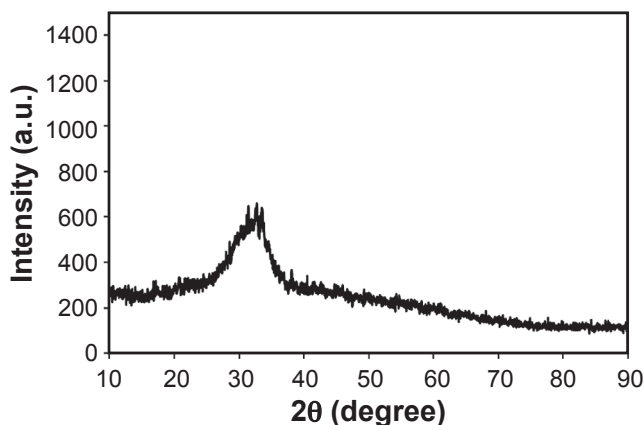


Figure 2: XRD pattern for BG.

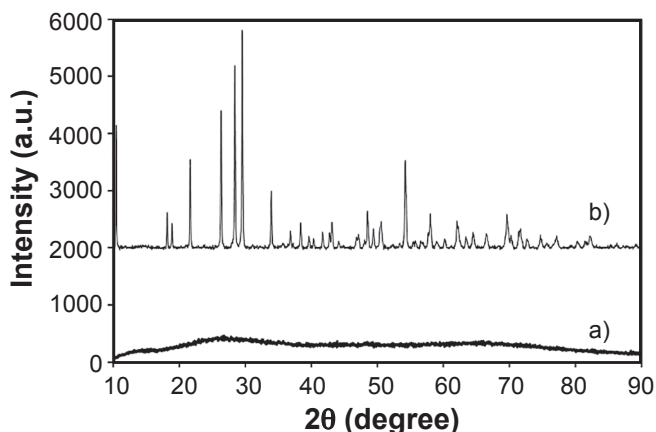


Figure 3: XRD patterns for cordierite powder before calcining and milling (a) and after calcining at $980^\circ\text{C}/2 \text{ h}$ (b).

Shrinkage: the shrinkage of the BG-cord composite was immediately measured after sintering at different sintering temperatures. Based on Fig. 4, the shrinkage of BG-cord increased from 8.94% (BG-C600) to 17.88% (BG-C925) when the sintering temperature was increased from 600 to 925°C . This showed that the shrinkage of BG-cord was greater at higher sintering temperatures. However, a sudden expansion was observed at the sintering temperature of 1000°C , as demonstrated by the negative shrinkage value of BG-C1000, indicating its expansion during sintering at this temperature.

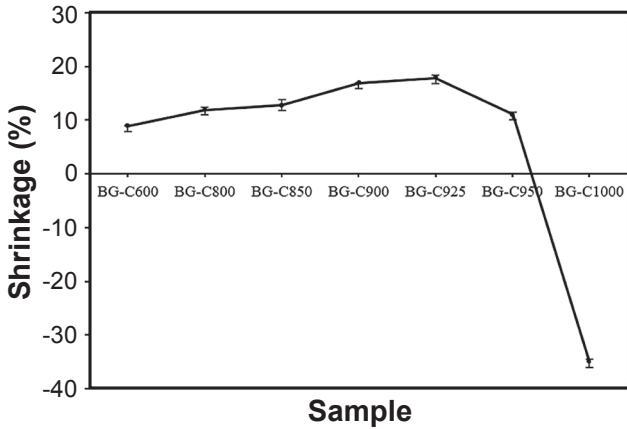


Figure 4: Shrinkage of BG-cord with different sintering temperatures.

Bulk density and porosity: based on Fig. 5, the bulk density increased from 1.94 to 2.52 g/cm³ when the sintering temperature was increased from 600 °C (BG-C600) to 950 °C (BG-C950). Meanwhile, the porosity of the BG-cord composite decreased from 24.24% to 1.96% when the sintering temperature was increased from 600 to 1000 °C (BG-C1000). The changes in the shrinkage, bulk density, and porosity values can be related to the densification and compacting effect. In a sintering process, particles are closely connected to each other and become compacted; so, at a higher sintering temperature, the connection between particles increases but the pore amount decreases [23]. Moreover, at a greater sintering temperature, crystallization is enhanced, therefore, particle readjustment takes place by viscous flow, and the particles become connected through sintering necks. This consequently affects the reduction of pore size in bioactive glass-ceramic samples, thus resulting in grain growth and increasing densification [24]. An increase in densification is also a result of the BG crystallization with increasing sintering temperature. The rearrangement of particles occurs during crystallization [25]. However, the shrinkage and bulk density of the composite drastically decreased to -35.03% (Fig. 4) and 1.59 g/cm³ (Fig. 5), respectively, after sintering

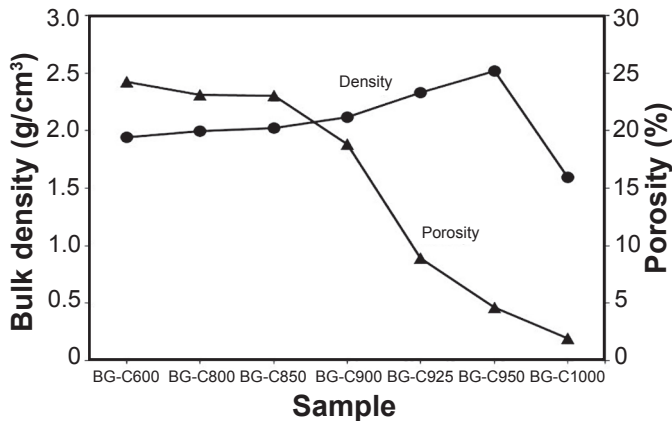


Figure 5: Bulk density and porosity of monolith BG-cord sintered at different temperatures.

at 1000 °C (BG-C1000). This was due to the bloating effect on the ceramic body. In addition, the formation of closed pores in the sample caused its expansion and bulk density reduction.

Microstructure: the microstructure of the BG-cord was observed as it was dependent on the sintering temperature. Moreover, the microstructure of a composite also affects its mechanical strength as well as its bioactivity performance. The microstructure of the BG-cord composite fabricated at different sintering temperatures was observed and the results are presented in Fig. 6. The BG-cord sintered at 600 °C had a lot of pores since the particles were yet to neck. This is because the driving force was not sufficient to bind the particles at this sintering temperature. At intermediate temperatures, the necking of particles was observed as the diffusion process took place and the amount of pores decreased with increasing sintering temperature from 800 to 900 °C. However, the formation of grain was not completed at this condition. This was due to the sufficient supply of sintering mechanism energy and the dominance of densification. This result corresponded with the result for porosity (Fig. 5), which decreased as the sintering

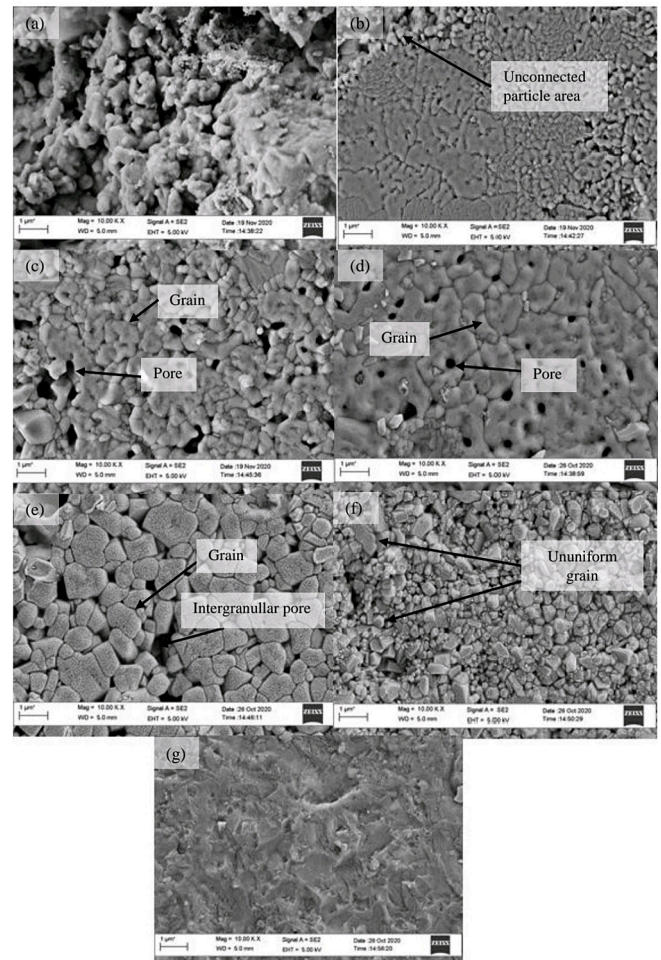


Figure 6: SEM micrographs of BG-cord sintered at different temperatures: a) 600 °C; b) 800 °C; c) 850 °C; d) 900 °C; e) 925 °C; f) 950 °C; and g) 1000 °C.

temperature increased. At a higher sintering temperature, the increasing driving force stimulated the growth of the neck between particles. On the other hand, the BG-cord sintered at 925 °C (BG-C925) demonstrated a complete necking and excellent grain growth with some intergranular pores. This finding was in agreement with a previous study by Leenakul *et al.* [24], whose particles are connected with increasing sintering temperature. However, non-uniform grain size and abnormal grain growth were observed in the BG-cord sintered at 950 °C. These microstructural discrepancies led to a lower strength as compared to BG-C925. When sintered at 1000 °C, the grain of the composite (BG-C1000) was difficult to observe as the composite crumbled. This phenomenon was due to the reaching of the melting temperature of the composite. In a conclusion, the grain behavior of ceramic is strongly dependent on its sintering temperature.

Diametral tensile strength (DTS): the correlation between DTS and porosity of the BG-cord at different sintering temperatures is presented in Fig. 7. The DTS increased from 14.01 to 30.54 MPa when the BG-cord was sintered from 600 to 925 °C. This was due to particle rearrangement leading to hardening of the surface and supporting grain growth. BG part in BG-cord, when sintered at lower temperatures, contained amorphous phase; when it was sintered at a higher temperature, it contained an additional secondary phase, combeite, promoting mechanical strength [24]. Moreover, the mechanical strength of ceramics also depends on porosity [23]. The ceramic bodies with lower porosity have fewer pores, exhibiting a greater tendency to withstand the force applied [26]. By increasing the connected particles, the greater the contact areas between the ceramic particles, which becomes the main reason for causing the improvement of mechanical strength due to the increase in the obstacle against the external force [27]. The increase in mechanical strength can also be explained by the BG-cord microstructure (Fig. 6). As the sintering temperature increases, particle necking rises and the densification dominates, which increases the mechanical strength. When sintered at 925 °C, the strength increase was higher because the necking of particles was completed and the good and

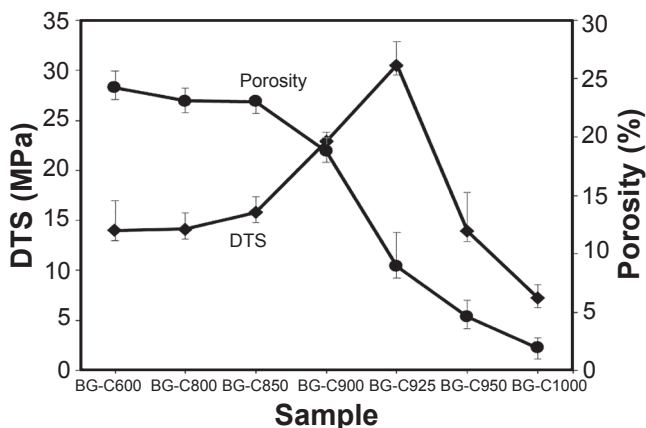


Figure 7: Correlation between diametral tensile strength (DTS) and porosity of BG-cord sintered at different temperatures.

uniform grain growth occurred at this sintering temperature.

However, the DTS decreased when the BG-cord was sintered up to 950 and 1000 °C. The change in slope was due to the presence of closed pores and the resulting bloating effect of the ceramic bodies [28]. When the sintering process continues and the temperature keeps increasing, the gases expand. The bloating effect caused an increase in closed porosity and poor surface quality [29]. As the sintered surface constrains the gas release, the growth of big bubbles in the core is presumably favored, with concomitant breakdown of septa and opening of a part of the initially closed pores [30]. The presence of closed pores resulted in a decrease in DTS. For getting a clear observation of this phenomenon, the micrographs of the cross-section of samples after sintering at 950 and 1000 °C are present in Fig. 8. Moreover, the grain of BG-cord sintered at 950 °C (BG-C950) was not uniform. Non-uniform grain growth results in low mechanical strength due to easier displacement to occur and the non-uniform grains are not efficient for blocking the effects of external force applied. From Fig. 8, the bloating effect can be clearly seen from the presence of pores inside the samples. The composite sintered at 950 °C (BG-C950) demonstrated a smaller pore size than that sintered at 1000 °C (BG-C1000). This observation corresponded with the DTS results, where the strength decreased when the samples were sintered up to 1000 °C (BG-C1000).

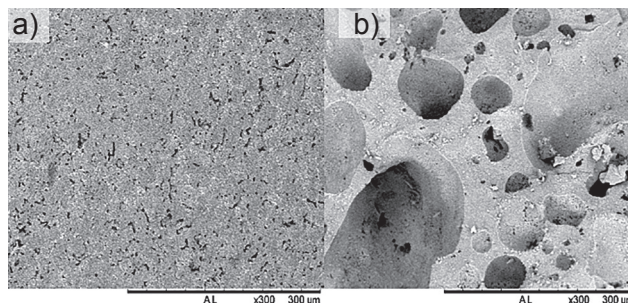


Figure 8: SEM images of the cross-section of BG-cord samples: a) BG-C950; and b) BG-C1000.

Bioactivity properties

The bioactivity of the BG-cord composite with a variation of sintering temperature was evaluated to observe the bioactive performance in response to increasing sintering temperature. Several analyses were conducted to observe the bioactivity of the BG-cord sintered at different temperatures, including SEM, XRD, and FTIR. The capability of apatite formation was observed and characterized in this evaluation.

SEM analysis: the apatite growth was observed using SEM on the BG-cord immersed for 7, 14, and 21 days in HBSS. The images of the BG-cord with a variation of sintering temperature before and after immersion in HBSS are presented in Figs. 9 to 15. The apatite formation was observed on BG-cord sintered at 600 to 950 °C after immersion in HBSS for 7 days. However, no apatite

formation was observed on the BG-C1000 after 7 days of immersion. After 14 and 21 days of immersion, apatite formation was observed on the BG-cord samples at all sintering temperatures including BG-C1000. It was proven that all of the samples sintered up to 1000 °C were bioactive. The formation of apatite in the physiological environment may be explained by a series of surface reactions involving exchanges of Na^+ or Ca^{2+} ions with H^+ or H_3O^+ ions from the solution at the material surface, formation of silanols (Si-OH) at the material-solution interface, migration of Ca^{2+} and PO_4^{3-} ions to the surface through the SiO_2 rich layer, formation of calcium phosphate layer, and crystallization of hydroxycarbonate apatite (HCA) by incorporating CO_3^{2-}

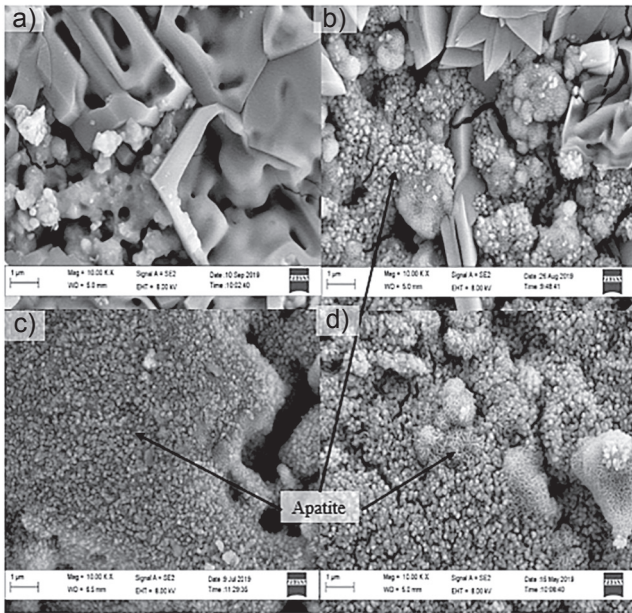


Figure 9: SEM images of BG-C600 surface after immersion in HBSS for 0 (a), 7 (b), 14 (c), and 21 (d) days.

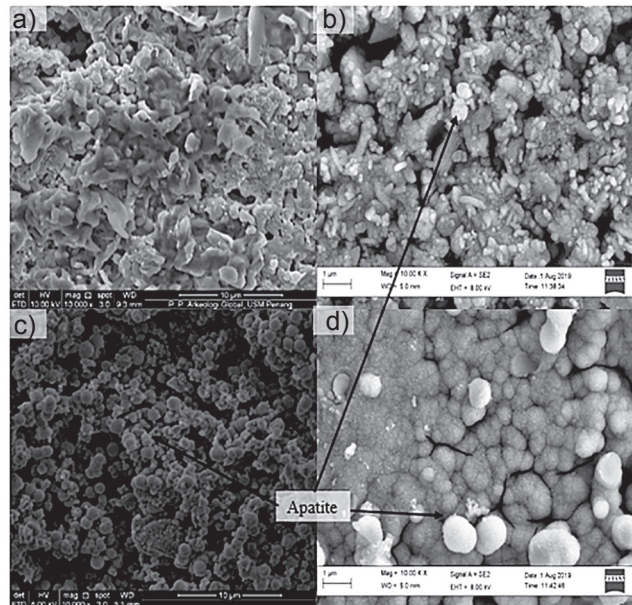


Figure 10: SEM images of BG-C800 surface after immersion in HBSS for 0 (a), 7 (b), 14 (c), and 21 (d) days.

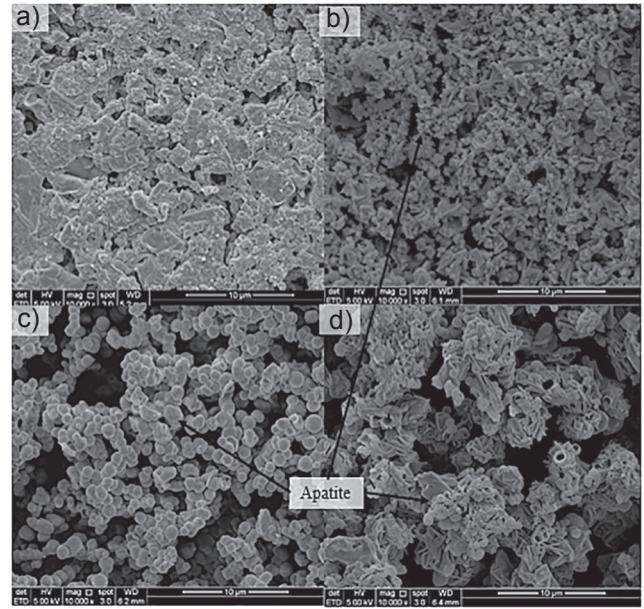


Figure 11: SEM images of BG-C850 surface after immersion in HBSS for 0 (a), 7 (b), 14 (c), and 21 (d) days.

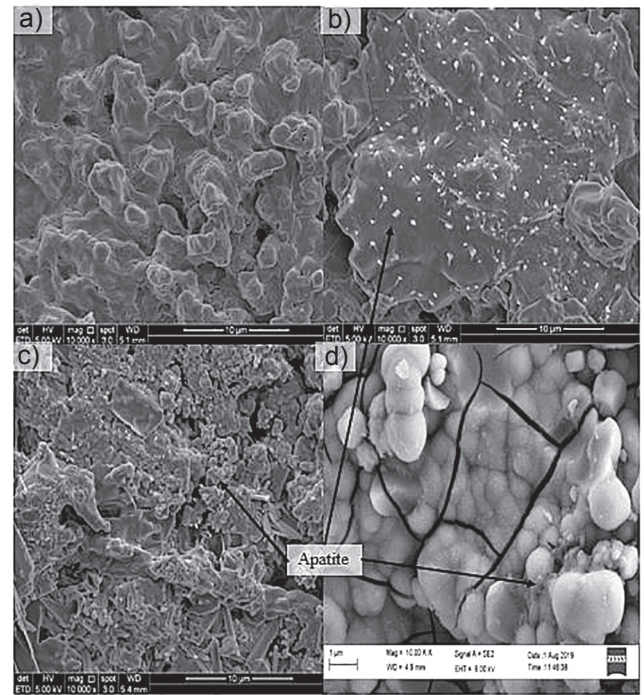


Figure 12: SEM images of BG-C900 surface after immersion in HBSS for 0 (a), 7 (b), 14 (c), and 21 (d) days.

ions [31]. The coverage area of apatite formation became wider with more obvious apatite formation observed after immersion up to 21 days. This elucidated that apatite nucleation and growth took place on the BG-cord surface at a longer immersion period.

However, the intensity of apatite formation on the surface of the BG-cord samples decreased when the sintering temperature increased. This was due to the decreasing bioactivity of the BG-cord at higher sintering temperatures. Moreover, the crystallinity of the samples increases when

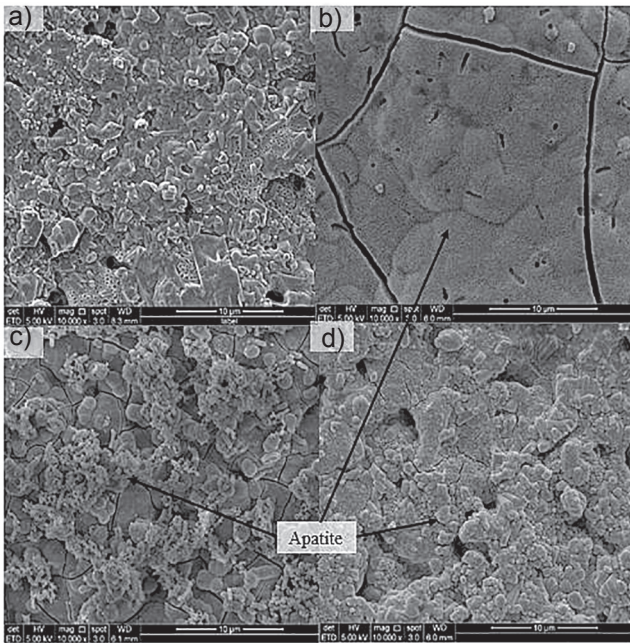


Figure 13: SEM images of BG-C925 surface after immersion in HBSS for 0 (a), 7 (b), 14 (c), and 21 (d) days.

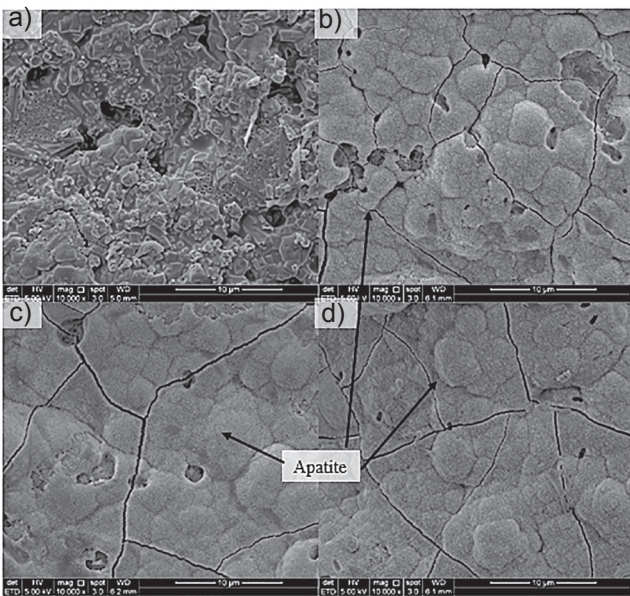


Figure 14: SEM images of BG-C950 surface after immersion in HBSS for 0 (a), 7 (b), 14 (c), and 21 (d) days.

the sintering temperature increases, resulting in lower bioactivity performance [32]. During the sintering process, the development of crystalline phases was observed from the formation of glass-ceramics. At higher sintering temperatures, the samples displayed a more intense crystalline phase. This lower glassy amorphous phase may also pose a negative effect on the bioactivity performance of the samples because the appearance of the crystalline phase hinders ions exchange and delays the formation of an apatite layer [24]. The crystalline structured atoms have a stronger bonding than in the glassy amorphous phase, which favors the dissolution process when being attacked by HBSS solution.

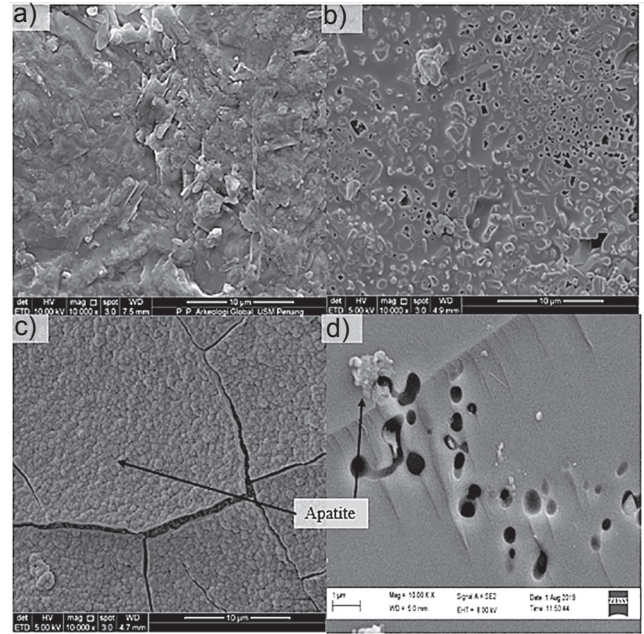


Figure 15: SEM images of BG-C1000 surface after immersion in HBSS for 0 (a), 7 (b), 14 (c), and 21 (d) days.

XRD analysis: the phases present in BG-cord sintered at different temperatures before and after immersion in HBSS were evaluated using XRD analysis, which results are present in Fig. 16. The XRD patterns for BG-C600 showed the presence of an amorphous phase, cordierite, and combeite. The intensity of the combeite phase peak became sharper due to the increasing BG crystallinity caused by increasing sintering temperature to 800 °C (BG-C800). The amount of BG crystallization was found to increase with increasing sintering temperature due to the higher energy gained by the atoms in BG to be properly arranged at higher sintering temperatures. The high amount of crystalline structure also contributed to high mechanical strength due to its well-arranged atoms. Crystalline materials consist of atoms of higher bonding energy that are able to withstand a higher load. With further increase in temperature to 850 and 900 °C, phases of pseudowollastonite [$\text{Ca}_3(\text{Si}_3\text{O}_9)$, ICDD 01-074-0874] and wollastonite (CaSiO_3 , ICDD 01-072-2297) were observed, respectively. Mirza et al. [33] also reported that the wollastonite phase appeared in the BG when sintered at 900 °C. On the other hand, at sintering temperatures of 925 °C (BG-C925), 950 °C (BG-C950), and 1000 °C (BG-C1000), the phase of larnite (Ca_2SiO_4) appeared. The presence of larnite in BG sintered above 900 °C is in agreement with a reported work [6]. It is worth mentioning that wollastonite and larnite have unique properties such as excellent bioactivity, nontoxicity, and good inducer of apatite formation [34, 35].

The XRD results of BG-cord after immersion in HBSS revealed phase changes on the surface of BG-cord for all sintering temperatures. The decreasing intensity of crystalline peaks of combeite and cordierite indicated the lower presence of the crystalline phase after immersion in HBSS. This change represented the degradation of

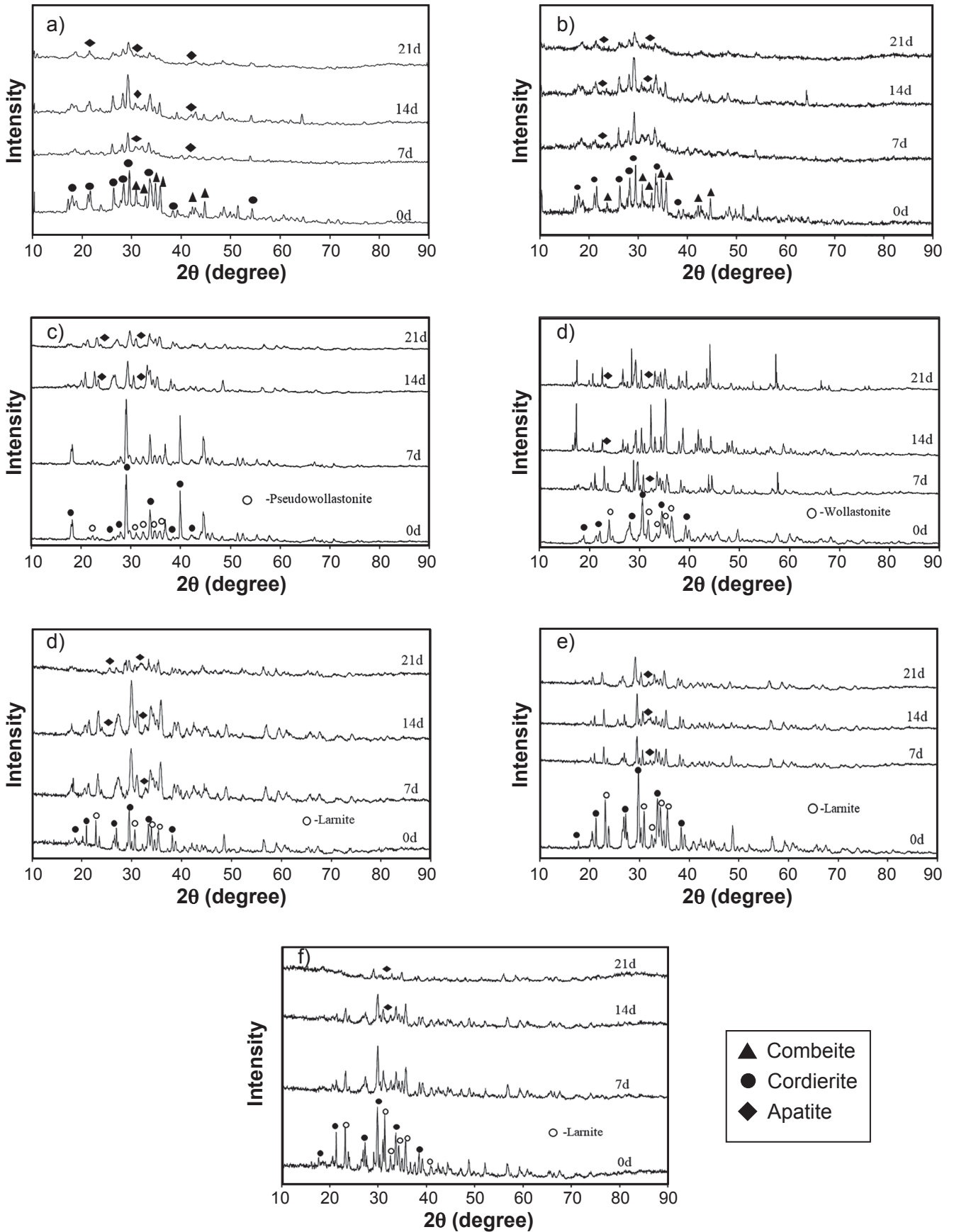


Figure 16: XRD patterns of BG-cord sintered at different temperatures: a) BG-C600; b) BG-C800; c) BG-C850; d) BG-C900; e) BG-C925; f) BG-C950; and g) BG-C1000.

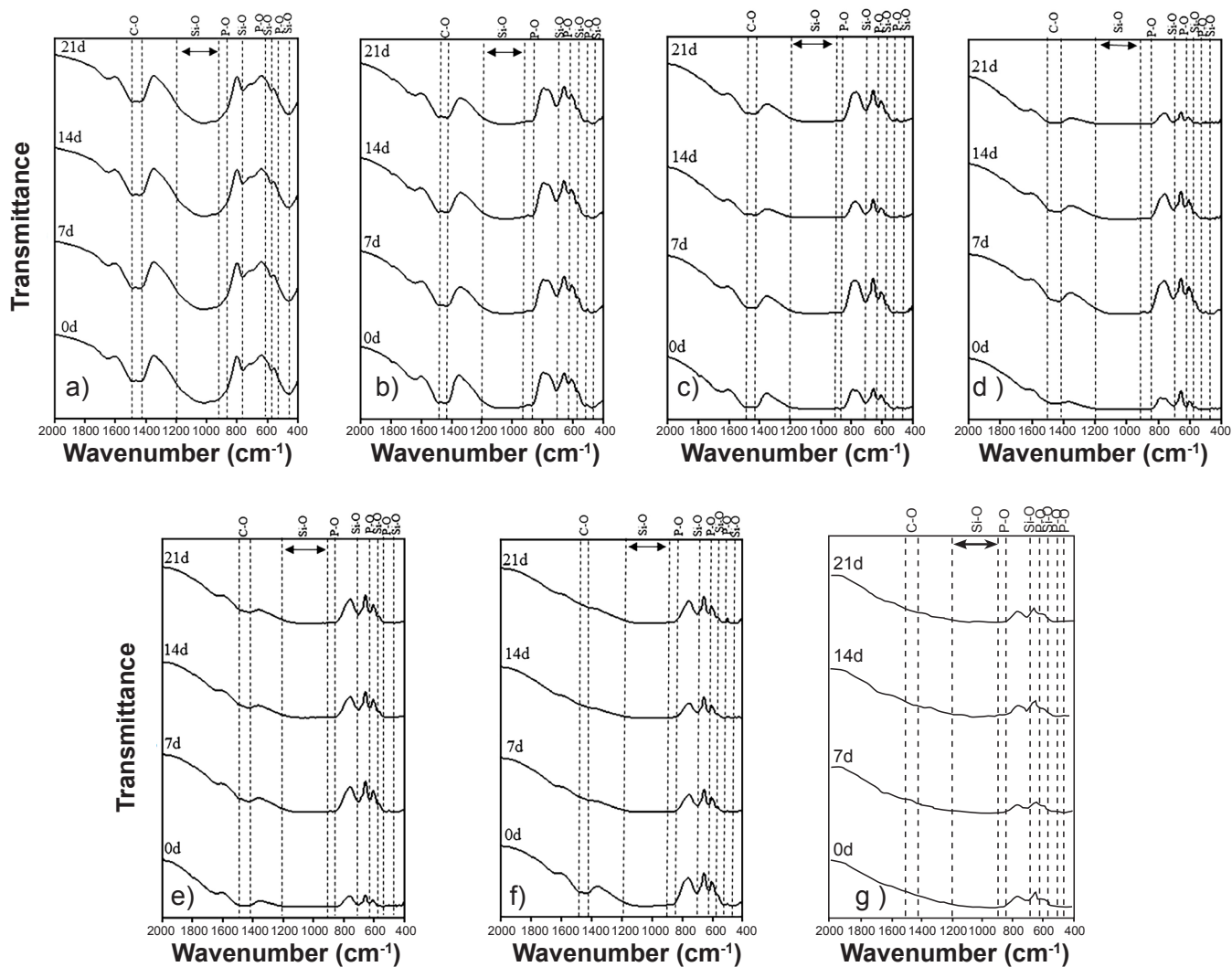


Figure 17: FTIR spectra of samples after immersing in HBSS: a) BG-C600; b) BG-C800; c) BG-C850; d) BG-C900; e) BG-C925; f) BG-C950; and g) BG-C1000.

combeite and cordierite in HBSS, which indirectly showed their biodegradable properties [36], even at high sintering temperatures. The apatite peaks were also observed after immersion in HBSS for 14 days. The appearance of low-intensity peaks in the XRD patterns indicated a significant formation of apatite on the sample surfaces. However, for most samples, the apatite peaks were unable to be observed due to overlapping with cordierite and combeite peaks.

Fourier transform infrared spectroscopy (FTIR): FTIR analyses were done on BG-cord sintered at different temperatures to observe the chemical bonding present, which results are shown in Fig. 17. The FTIR spectra of all samples indicated the characteristics of the silica network representative of the silicate bioactive glass. The band was located in the range of 421 to 505 cm^{-1} corresponding to the Si-O-Si bending mode. Mg-O peak was observed at 575 cm^{-1} from cordierite composition [37]. The peaks around 590 and 875 cm^{-1} represent P-O bending mode in the PO_4^{3-} groups, while the peak around 750 cm^{-1} was attributed to the Si-O-Si symmetric stretching vibration of bridging oxygen atom. The

broad peak from 900 to 1200 cm^{-1} on the other hand was assigned to the Si-O-Si asymmetric vibration [9, 38, 39]. Meanwhile, the band located at 1426 cm^{-1} was associated with the carbonate group stretching vibration mode [4]. However, the band of the carbonate group was broader and less intense for the samples sintered at 950 and 1000 $^{\circ}\text{C}$, probably due to the decrease in the apatite formation performance at high temperatures.

After the bioactivity test, new peaks appeared between 610 and 620 cm^{-1} and at around 525 cm^{-1} , representing the P-O mode and crystalline P-O group, respectively. Meanwhile, the peaks around 590 and 715 cm^{-1} were observed to be more intense [40]. The high-intensity peak at 715 cm^{-1} revealed the formation of silanol group (silica-rich layer) on the sample surface after immersion in HBSS, which was due to the exchange of sodium and calcium ions with hydrogen ions between HBSS and the samples [41]. The twin peaks around 1426 and 1490 cm^{-1} also became more intense due to the migration of calcium and phosphorus ions from HBSS to the samples to form amorphous $\text{CaO-P}_2\text{O}_5$ [42]. The changes

in the FTIR spectra before and after immersion in HBSS showed the successful formation of apatite on the samples' surface.

CONCLUSIONS

Bioactive glass and cordierite (BG-cord) composite was successfully fabricated using a variation of sintering temperature (600 to 1000 °C). A positive improvement in the mechanical properties of the BG-cord composite was observed from the high diametral tensile strength (DTS) values with cordierite incorporation. Overall, the BG-cord sintered at 925 °C (BG-C925) demonstrated the highest DTS value (30.54 MPa). In the evaluation of the bioactivity performance, the formation of an apatite layer on the BG-cord composite surface as observed from SEM images proved that the composite was bioactive. Therefore, the BG-cord composite is found convenient to be utilized in the load-bearing orthopedic area since it promotes high mechanical strength and bioactivity response.

ACKNOWLEDGEMENTS

The authors would like to convey thanks to Assoc. Prof. Dr. Hasmaliza Mohamad for her useful and supportive suggestions during the preparation of this research work. The Ministry of Higher Education supported this work by sponsoring this research work with FRGS Grant (6071423). The authors would also like to extend their recognition to the Ministry of Higher Education Malaysia and the School of Materials and Mineral Resources Engineering, Universiti Sains Malaysia, for contribution to this research.

REFERENCES

- [1] J. Yao, S. Radin, P.S. Leboy, P. Ducheyne, *Biomaterials* **26** (2005) 14.
- [2] W. Höland, V. Rheinberger, E. Apel, E.C. Van't Hoen, M. Höland, A. Dommann, M. Obrecht, C. Mauth, U. Graf-Hausner, *J. Mater. Sci. Mater. Med.* **17** (2006) 11.
- [3] Q. Yao, P. Nooeaid, J.A. Roether, Y. Dong, Q. Zhang, A.R. Boccaccini, *Ceram. Int.* **39** (2013) 7.
- [4] N.F. Ibrahim, H. Mohamad, S.N.F.M. Noor, *J. Non-Cryst. Solids* **462** (2017) 23.
- [5] K. Zhang, Q. Van Le, *Compos. Compd.* **2** (2020) 10.
- [6] H. Ghomi, M.H. Fathi, H. Edris, *Mater. Res. Bull.* **47**, 11 (2012) 3523.
- [7] A. Ardeshiryajimi, S. Farhadian, F.J. Adegani, S. Mirzaei, M.S. Zomorrod, L. Langroudi, A. Doostmohammadi, E. Seyedjafari, M. Soleimani, *Cell Prolif.* **48**, 4 (2015) 455.
- [8] V. Anand, K.J. Singh, K. Kaur, *J. Non. Cryst. Solids* **406** (2014) 88.
- [9] L.A. Adams, E.R. Essien, A.T. Adesalu, M.L. Julius, *J. Sci. Adv. Mater. Dev.* **2**, 4 (2017) 476.
- [10] M. Montazerian, E.D. Zanotto, *J. Biomed. Mater. Res. A* **104**, 5 (2016) 1231.
- [11] V. Miguez-Pacheco, L.L. Hench, A.R. Boccaccini, *Acta Biomater.* **13** (2015).
- [12] Z. Barbara, D. Michal, O. Zbigniew, C. Katarzyna, L. Maria, *Ceram. Int.* **43** (2017) 12742.
- [13] J.R. Jones, *Acta Biomater.* **9**, 1 (2013) 4457.
- [14] D. Bellucci, A. Sola, L. Lusvardi, V. Cannillo, *Ceram. Int.* **40**, 2 (2014) 3805.
- [15] Y. Guojing, Y. Xianyan, Z. Lei, L. Mian, S. Xiaoliang, C. Xiaoyi, G. Zhongru, *Mater. Lett.* **75** (2012) 80.
- [16] T. Kokubo, H.M. Kim, M. Kawashita, *Biomaterials* **24**, 13 (2003) 2161.
- [17] M.M.S. Sanad, M.M. Rashad, E.-S. Abdel-Aal, M.F. El-Shahat, K.W. Powers, *Int. J. Appl. Ceram. Technol.* **11**, 5 (2014) 864.
- [18] P. Mengucci, G. Majni, A. De Benedittis, G. Biagini, *Biomaterials* **19** (1998) 1447.
- [19] A. Krajewski, A. Ravaglioli, M. Kirsch, G. Biagini, R. Solmi, M. Belmonte, C. Zucchini, M.G. Gandolfi, C. Castaldini, L. Rodriguez, R. Giardino, R. Mongiorgi, E. Roncari, L. Orlandi, *J. Mater. Sci. Mater. Med.* **7**, 2 (1996) 99.
- [20] L. Orlandi, R. Solmi, A. Krajew, A. Bearzatto, G. Biagini, E. Ciccopiedil, A. Ravaglioli, *Biomaterials* **18**, 14 (1997) 955.
- [21] J. Ma, C.Z. Chen, D.G. Wang, J.H. Hu, *Ceram. Int.* **37**, 5 (2011) 1637.
- [22] K. Morinaga, H. Takebe, *High Temp. Mater. Process.* **22** (2003) 3.
- [23] L.F. Hu, C.A. Wang, *Ceram. Int.* **36**, 5 (2010) 1697.
- [24] W. Leenakul, T. Tunkasiri, N. Tongsi, K. Pengpat, J. Ruangsuriya, *Mater. Sci. Eng. C* **61** (2016) 695.
- [25] O.P. Filho, G.P. Latorre, L.L. Hench, *J. Biomed. Mater. Res.* **30**, 4 (1996) 509.
- [26] B. Thavornyutikarn, P. Tesavibul, K. Sitthiseripratip, N. Chatarapanich, B. Feltis, P.F.A. Wright, T.W. Turney, *Mater. Sci. Eng. C* **75** (2017) 1281.
- [27] Y.S. Han, J.B. Li, Q.M. Wei, K. Tang, *Ceram. Int.* **28**, 7 (2002) 755.
- [28] H. Badiie, A. Maghsoudipour, B.R. Dehkordi, *Adv. Appl. Ceram.* **107**, 2 (2008) 111.
- [29] E. Bou, M.F. Quereda, D. Lever, A.R. Boccaccini, C.R. Cheeseman, *Adv. Appl. Ceram.* **108**, 1 (2009) 44.
- [30] C. Molinari, C. Zanelli, G. Guarini, M. Dondi, *Constr. Build. Mater.* **261** (2020) 119980.
- [31] M.U. Hashmi, S.A. Shah, F. Umer, A.S. Alkedy, *Ceram.-Silik.* **57**, 4 (2013) 313.
- [32] J.P. Nayak, J. Bera, *Appl. Surf. Sci.* **257**, 2 (2010) 458.
- [33] A. Mirza, M. Riaz, R. Zia, T. Hussain, F. Bashir, *J. Alloys Compd.* **726** (2017) 348.
- [34] S.S. Hossain, S. Yadav, S. Majumdar, S. Krishnamurthy, R. Pyare, P.K. Roy, *Ceram. Int.* **46**, 1 (2020) 833.
- [35] S.K. Venkatramana, R. Choudhary, G. Krishnamurthy, H.R.B. Raghavendran, M.R. Muralic, T. Kamarul, A. Suresh, J. Abraham, S. Swamiappan, *Mater. Sci. Eng. C* **118** (2020) 111466.
- [36] S. Herradi, S. Bouhazma, S. Chajri, M. Khaldi, A. El Hachadi, B. El Bali, M. Lachkar, *J. Phys. Conf. Ser.* **984**, 1 (2018).

- [37] R. Petrović, D. Janačković, S. Zec, S. Drmanić, L. Kostić-Gvozdrenović, J. Sol-Gel Sci. Technol. **28**, 1 (2003) 111.
- [38] J. Faure, R. Drevet, A. Lemelle, N. Ben Jaber, A. Tara, H. El Btaouri, H. Benhayoune, Mater. Sci. Eng. C **47** (2015) 407.
- [39] T. Himanshu, S.P. Singh, K.A. Sampath, M. Prerna, J. Ashish, Bioceram. Dev. Appl. **6**, 1 (2016) 6.
- [40] V.K. Vyas, A.S. Kumar, P. Sunil, S.P. Singh, R. Pyare, Bull. Mater. Sci. **38**, 4 (2015) 957.
- [41] X.V. Bui, T.H. Dang, Process. Appl. Ceram. **13**, 1 (2019) 98.
- [42] N. Farhana, H. Mohamad, S. Noor, F. Mohd, N. Ahmad, Ceram. Int. **43**, 15 (2017) 11676.
(*Rec.* 26/01/2021, *Rev.* 13/06/2021, *01/08/2021*, *Ac.* 09/08/2021)

